Growth hormone-releasing hormone agonists ameliorate chronic kidney disease-induced heart failure with preserved ejection fraction

Angela C. Rieger[a], Luiza L. Bagno[a], Alessandro Salerno[a], Victoria Florea[a], Jose Rodriguez[a], Marcos Rosado[a], Darren Turner[a], Raul A. Dulce[a], Lauro M. Takeuchi[a], Rosemeire M. Kanashiro-Takeuchi[a,b], Peter Buchwald[b,c], Amarylis C. B. A. Wanschel[a], Wayne Balkan[a,d], Ivonne H. Schulman[a,d,e], Andrew V. Schally[c,d,f,1], and Joshua M. Hare[a,d,1]

[a]Interdisciplinary Stem Cell Institute, University of Miami Miller School of Medicine, Miami, FL 33136; [b]Department of Molecular and Cellular Pharmacology, University of Miami Miller School of Medicine, Miami, FL 33136; [c]Diabetes Research Institute, University of Miami Miller School of Medicine, Miami, FL 33136; [d]Department of Medicine, University of Miami Miller School of Medicine, Miami, FL 33136; [e]Katz Family Division of Nephrology and Hypertension, University of Miami Miller School of Medicine, Miami, FL 33136; and [f]Endocrine, Polypeptide and Cancer Institute, Veteran Affairs Medical Center, Miami, FL 33125

Contributed by Andrew V. Schally, December 4, 2020 (sent for review September 23, 2020; reviewed by Wilson Colucci and Lior Gepstein)

Therapies for heart failure with preserved ejection fraction (HFpEF) are lacking. Growth hormone-releasing hormone agonists (GHRH-As) have salutary effects in ischemic and nonischemic heart failure animal models. Accordingly, we hypothesized that GHRH-A treatment ameliorates chronic kidney disease (CKD)-induced HFpEF in a large-animal model. Female Yorkshire pigs (n = 16) underwent 5/6 nephrectomy via renal artery embolization and 12 wk later were randomized to receive daily subcutaneous injections of GHRH-A (MR-409; n = 8; 30 μg/kg) or placebo (n = 8) for 4 to 6 wk. Renal and cardiac structure and function were serially assessed postembolization. Animals with 5/6 nephrectomy exhibited CKD (elevated blood urea nitrogen [BUN] and creatinine) and faithfully recapitulated the hemodynamic features of HFpEF. HFpEF was demonstrated at 12 wk by maintenance of ejection fraction associated with increased left ventricular mass, relative wall thickness, end-diastolic pressure (EDP), end-diastolic pressure/end-diastolic volume (EDP/EDV) ratio, and tau, the time constant of isovolumic diastolic relaxation. After 4 to 6 wk of treatment, the GHRH-A group exhibited normalization of EDP (P = 0.03), reduced EDP/EDV ratio (P = 0.018), and a reduction in myocardial pro-brain natriuretic peptide protein abundance. GHRH-A increased cardiomyocyte [Ca^{2+}] transient amplitude (P = 0.009). Improvement of the diastolic function was also evidenced by increased abundance of titin isoforms and their ratio (P = 0.0022). GHRH-A exerted a beneficial effect on diastolic function in a CKD large-animal model as demonstrated by improving hemodynamic, structural, and molecular characteristics of HFpEF. These findings have important therapeutic implications for the HFpEF syndrome.

cardiorenal syndrome | chronic kidney disease | heart failure with preserved ejection fraction | large animal model

The prognosis for heart failure with preserved ejection fraction (HFpEF), a complex clinical syndrome involving multiple comorbidities with limited treatment options (1–3), has not improved over decades, and numerous drug classes that are effective for heart failure with reduced ejection fraction (HFrEF) have, to date, shown limited to no clinical benefits in HFpEF (4–7). In addition, the relative scarcity of animal models (8–10) impedes discovery of novel therapies for HFpEF. One important cause of HFpEF is chronic kidney disease (CKD), which has among the worst outcomes of the HFpEF syndromes (11). It manifests predominantly with pathologic left ventricle (LV) remodeling characterized by LV hypertrophy with increased LV-mass index and relative wall thickness (RWT), impaired ventricular arterial coupling, right ventricular relaxation, and increased stroke work (SW) (11).

Growth hormone-releasing hormone (GHRH) is a pleiotropic hormone that has extrapituitary effects, exerted via activation of GHRH receptors (12–15). In murine models of ischemic cardiomyopathy (ICM) with reduced ejection fraction (EF) (13), GHRH agonists (GHRH-As) improve cardiac function and decrease scar size, mediated by myocardial GHRH receptor activation (14, 15). Importantly, GHRH actions in the heart are independent of the

Significance

This randomized, blinded study used rigorous hemodynamic tools to test the efficacy of a synthetic growth hormone-releasing hormone agonist (GHRH-A) on the restoration of diastolic function in a large animal model of chronic kidney disease (CKD)-induced heart failure with preserved ejection fraction (HFpEF). CKD was produced in Yorkshire swine by performing a 5/6 nephrectomy via catheter-based renal artery embolization. HFpEF was evident at 12 wk postembolization. Daily injection of GHRH-A improved cardiac diastolic hemodynamics, including end-diastolic pressure, end-diastolic pressure–volume ratio, and stroke work, compared to placebo. Development of this swine model and therapeutic approach has important implications because of the high prevalence of CKD-induced HFpEF and cardiorenal syndromes, lack of effective therapies, and few large-animal models available for investigation.

Author contributions: A.C.R., W.B., I.H.S., and J.M.H. designed research; A.C.R., L.L.B., A.S., V.F., J.R., M.R., R.A.D., L.M.T., R.M.K.-T., and A.C.B.A.W. performed research; A.V.S. contributed new reagents/analytic tools; A.C.R., L.L.B., A.S., V.F., J.R., D.T., R.A.D., L.M.T., R.M.K.-T., P.B., and A.C.B.A.W. analyzed data; and A.C.R., L.L.B., R.A.D., R.M.K.-T., W.B., I.H.S., and J.M.H. wrote the paper.

Reviewers: W.C., Boston University School of Medicine; and L.G., Technion–Israel Institute of Technology.

Competing interest statement: A.V.S and J.M.H. are listed as co-inventors on patents on GHRH analogs, which were assigned to the University of Miami and Veterans Affairs Department. J.M.H. previously owned equity in Biscayne Pharmaceuticals, licensee of intellectual property used in this study. Biscayne Pharmaceuticals did not provide funding for this study. J.M.H. is the chief scientific officer, a compensated consultant, and advisory board member for Longeveron and holds equity in Longeveron. J.M.H. is also the co-inventor of intellectual property licensed to Longeveron. Longeveron did not play a role in the design, conduct, or funding of the study. J.M.H.'s relationships are reported to the University of Miami, and an appropriate management plan is in place. I.H.S. contributed to this manuscript in her personal capacity. The opinions expressed in this article are the author's own and do not reflect the view of the National Institutes of Health, the Department of Health and Human Services, or the United States government.

[1]To whom correspondence may be addressed. Email: andrew.schally@va.gov or jhare@med.miami.edu.

This article contains supporting information online at https://www.pnas.org/lookup/suppl/doi:10.1073/pnas.2019835118/-/DCSupplemental.

Published January 19, 2021.

growth hormone–IGF1 axis (16). Further mechanisms of action include decreased apoptosis of cardiomyocytes and inflammatory responses (14, 17). The GHRH-A, MR-409, improved diastolic strain and reduced myocardial scar in a swine large-animal model with subacute ICM (12). Notably, in a murine HFpEF model using chronic administration of angiotensin II, GHRH-A prevented impairment of cardiomyocyte contractile function and relaxation and development of HFpEF features, including LV hypertrophy, collagen deposition, and diastolic dysfunction compared to placebo (18). Here, we developed a large-animal model of HFpEF using swine with CKD-induced HFpEF, a model that faithfully recapitulated the hemodynamic characteristics observed in humans, to test the hypothesis that GHRH-A ameliorates cardiac diastolic dysfunction.

Results

Animal Model. For this study, we employed a large-animal model of 5/6 nephrectomy (19) with hemodynamic features of HFpEF. CKD was evident 12 wk following renal artery embolization by increased creatinine (Δ1.09 ± 0.13 mg/dL; $P < 0.0001$) (Table 1 and *SI Appendix*, Fig. S1*A*) and blood urea nitrogen (BUN) (Δ10.38 ± 1.31 mg/dL; $P < 0.0001$) (*SI Appendix*, Fig. S1*B*). Hemoglobin decreased [−2.9 ± 0.4 mg/dL; $P < 0.0001$)] (*SI Appendix*, Fig. S1*C*) and mean arterial pressure (MAP) increased by 7.4 ± 3.3 mmHg ($P = 0.04$) (*SI Appendix*, Fig. S1*D*).

Hemodynamic features of HFpEF developed in the model at 12 wk following nephrectomy. At this time, there was an increased left ventricular end-diastolic (LVED) mass corrected by body surface area (BSA) (34.79 ± 8.11 g/m^2; $P = 0.0002$; *SI Appendix*, Fig. S2), elevated RWT by 0.12 ± 0.02 mm ($P < 0.0001$); *SI Appendix*, Fig. S2 *B* and *C*), end-diastolic pressure (EDP) by 8.9 ± 2.4 mmHg ($P = 0.002$; Fig. 1*A*), EDP/end-diastolic volume (EDV) ratio/BSA by 0.09 ± 0.02 mmHg/mL/m^2 ($P = 0.002$; Fig. 1*B*), and tau by 25.9 ± 9.6 ms ($P = 0.001$; Fig. 1*C*). EF was maintained within the normal range throughout the study (20). At 12 wk postembolization, one animal was inducible for ventricular tachycardia in response to programmed electrical stimulation and was not successfully resuscitated.

Response to GHRH. Animals were then randomly assigned to receive daily subcutaneous GHRH-A (MR-409; 30 μg/kg) or placebo. GHRH-A administration improved indices of renal and cardiac function. At study completion, BUN was significantly lower, by 6.6 ± 2.3 mg/dL ($P = 0.019$) in GHRH-A– compared to placebo-treated animals (placebo, 23.0 ± 0.9 mg/dL, vs. GHRH-A, 16.3 ± 0.6 mg/dL, at 16 to 18 wk postembolization). Creatinine (placebo, 2.6 ± 0.1 mg/dL, vs. GHRH-A, 2.1 ± 0.07 mg/dL, at 16 to 18 wk postembolization), MAP (placebo, 73.5 ± 5.5 mmHg, vs. GHRH-A, 71.5 ± 5.4 mmHg, at 16 to 18 wk postembolization), anemia (Hematocrit: placebo, 26.8 ± 0.4 [%], vs. GHRH-A, 24.4 ± 0.4 [%], at 16 to 18 wk postembolization), and EF (placebo, 52 ± 0.9 [%], vs. GHRH-A, 51 ± 0.6 [%], at 16 to 18 wk postembolization) were not different between groups.

Table 1. Laboratory parameters from baseline and 12 wk postembolization demonstrating establishment of the CKD-induced model prior to treatment

		12 wk postembolization		
Laboratory parameters	Baseline	Placebo	GHRH-A	*P* value
Renal function				
MAP, mmHg	64.8 ± 4.0	73.5 ± 4.2*	71.5 ± 7.4*	0.04
Creatinine, mg/dL	1.3 ± 0.1	2.7 ± 0.2*	2.2 ± 0.2*	0.0001
BUN, mg/dL	9.2 ± 0.6	22.9 ± 2.8*	16.2 ± 1.8*	<0.0001
Hematology				
Hgb, mg/dL	10.2 ± 0.3	8.4 ± 0.3*	7.7 ± 0.3*	<0.0001
HCT, %	33.6 ± 0.3	27 ± 0.4*	24.3 ± 0.4*	<0.0001

The values at 12-wk postembolization are divided according to the subsequent treatment. BUN, blood urea nitrogen; HCT, hematocrit; Hgb, hemoglobin; MAP, mean arterial pressure. *P* values refer to analysis within groups throughout the model establishment, paired *t* test. No difference between groups at 12 wk postembolization time point. All data are expressed as mean ± SEM. * indicates statistical significance compared to Baseline. Two-way ANOVA; *P* values are shown in the last column.

GHRH-A administration restored diastolic function toward normal. Importantly, EDP fell by −9.3 ± 3.8 mmHg ($P = 0.027$) and was associated with recovered passive diastolic function and decreased (EDP/EDV) ratio/BSA of 0.09 ± 0.02 mmHg/mL/m^2 ($P = 0.018$; Fig. 2 *A* and *B*). Active relaxation, as characterized by tau and isovolumetric relaxation, as measured by dP/dt_{min}, were both improved in the GHRH-A group, but were not significantly different between groups (Fig. 2 *C* and *D*). SW increased over time in the placebo group by 1,482 ± 349.8 mmHg·mL ($P = 0.0007$; Fig. 2*E*). Preload recruitable stroke work (PRSW) and dP/dt_{max} were similar between groups with no changes over time.

The percent change from baseline of LVED-Mass/BSA at the end of the study between the placebo (51.6 ± 5.3%) and GHRH-A (44.6 ± 4.3%) groups was not significantly different (Fig. 2*F*) (Table 2). Importantly, there was a trend for GHRH-A to ameliorate progression of LV hypertrophy: The increase in LVED-Mass/BSA during treatment (between weeks 12 and 16 to 18) was greater in the placebo-treated (9.6 ± 1.6%) than in the GHRH-A–treated (3.0 ± 1.4%) animals. RWT (Fig. 2*G*), EDV, ESV, stroke volume (SV) corrected by BSA, and dry lung weight (placebo, 42.5 ± 3.6 g, vs. GHRH-A, 41.9 ± 3.3 g; $P = 0.91$) were similar between the two groups. Ventricular tachycardia was reproduced by electrical stimulation in one animal of the placebo group but none from the GHRH group.

Next, we assessed the intracellular calcium ($[Ca^{2+}]$) handling in cardiomyocytes isolated at the end of the study. The $[Ca^{2+}]$ transient amplitude was increased ($P = 0.009$) in cardiomyocytes from GHRH-A–treated animals (Fig. 3 *A* and *B*). Although Ca^{2+} release was faster in the placebo group when paced at 0.2 Hz, no differences were evident at any other frequencies, as shown by time to reach $[Ca^{2+}]$ peak (ttp) (Fig. 3 *A*, *Left*, and *C*) or $d[Ca^{2+}]/dt_{max}$ (Fig. 3*D*). There were also no differences in the rate of Ca^{2+} decay as assessed by the time from the peak toward the baseline (bsl) (time to 10% bsl, 50% bsl and 90%) (Fig. 3 *E*–*G*) or $d[Ca^{2+}]/dt_{min}$ (Fig. 3*H*). The dose–response to isoproterenol of intracellular Ca^{2+} was also not significantly affected in cardiomyocytes derived from GHRH-A–treated compared with placebo-treated animals (Fig. 3*I*). We used tetracaine to indirectly assess the sarcoplasmic reticulum (SR) Ca^{2+} leak in these cardiomyocytes. We plotted the load–leak pairs and found no differences between curves (although a lower $SRCa^{2+}$ leak appears to be induced by GHRH-A treatment, at low levels of $SR[Ca^{2+}]$ content only; Fig. 3*J*). There was no significant difference in early afterdepolarization and other arrhythmogenic behaviors (21) between placebo- and GHRH-A–treated cardiomyocytes (*SI Appendix*, Fig. S3).

To determine whether myocardial fibrosis was associated with this CKD-induced swine model of HFpEF, we assessed collagen I and III content by Western blot analysis and Picro Sirius Red staining. Neither of these approaches demonstrated a significant difference in these collagens between placebo- and GHRH-treated hearts (*SI Appendix*, Fig. S4).

Next, we examined molecular correlates of myocyte stiffness and ventricular wall stress. We measured the abundance of titin isoforms, which contribute directly to passive cardiomyocyte tension; N2B is the cardiac-specific, shorter, and stiffer isoform, while N2BA is the longer and more compliant isoform (22). Activated titin isoforms (phosphorylated N2BA and N2B) were decreased in the placebo group compared to controls and the GHRH-A–treated group (Fig. 4*A*). The N2BA/N2B ratio in the LV of

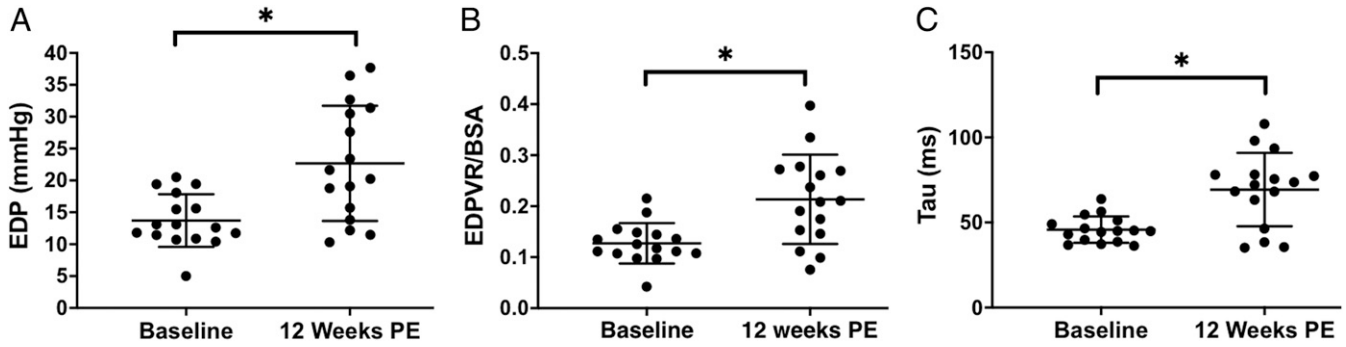

Fig. 1. Diastolic hemodynamic parameters, 12 wk following renal embolization. Diastolic dysfunction, a key sign of HFpEF, is evident as shown by increased (*A*) end-diastolic pressure (EDP) (*$P = 0.002$), (*B*) EDP/end-diastolic volume (EDV) ratio/BSA (*$P = 0.002$), and (*C*) tau by (*$P = 0.001$). All data are expressed as mean ± SEM.

the GHRH-A group was significantly increased compared to the placebo ($P = 0.011$, Fig. 4*A*), consistent with GHRH-A administration contributing to reduced titin stiffness and improved diastolic LV function in HFpEF. We also assessed the levels of pro-BNP by Western blot analysis in the myocardium of control (naive animals) and placebo- and GHRH-A–treated HFpEF hearts, to index wall stress (23). Whereas placebo-treated animals exhibited significantly elevated pro-BNP expression compared to control animals, the level of myocardial pro-BNP was restored toward normal in GHRH-A–treated animals ($P = 0.003$; Fig. 4*B*).

Cardiac chemo/cytokines can promote hypertrophy (24–26). The inflammatory marker, macrophage chemotactic peptide-1 (MCP-1), encoded by the gene *CCL2*, is associated with increased myocyte apoptosis and ventricular dysfunction (27). We

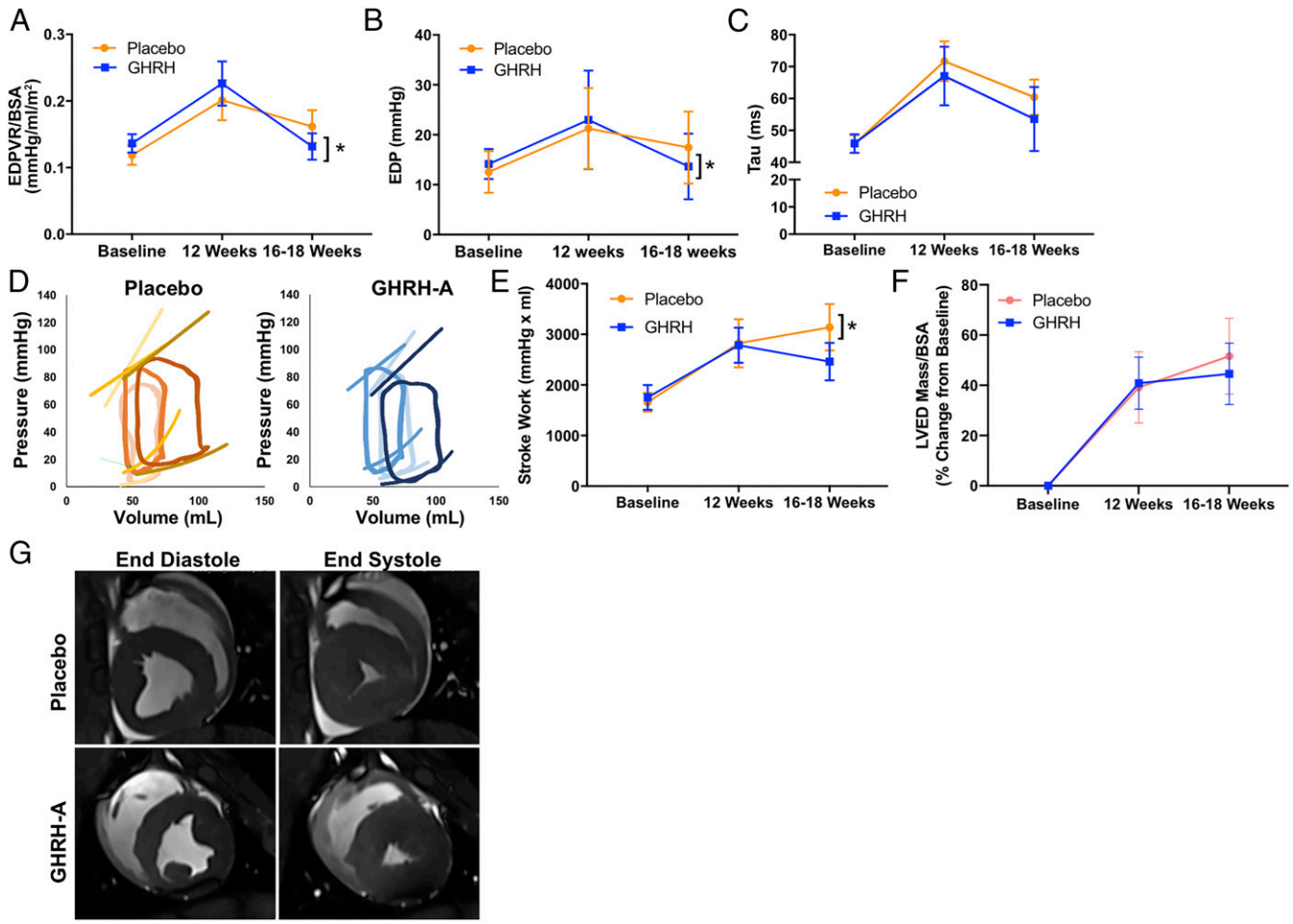

Fig. 2. Impact of GHRH-A on the HFpEF phenotype. GHRH-A improves diastolic function including the following: (*A*) EDP/EDV corrected by BSA, (*B*) EDP, and (*C*) tau. (*D*) Representative PV loops (GHRH-A, blue; placebo, orange; baseline, light color; 12 wk PE, bright color; 18 wk PE, dark color). As depicted, animals maintain EF but develop an increased end-diastolic pressure–volume relationship consistent with HFpEF. CKD-HFpEF phenotype presents with increased (*E*) SW, (*F*) left ventricular end-diastolic (LVED) mass/BSA, and (*G*) representative cardiac MRI showing increased relative wall thickness (RWT) following renal embolization. All data are expressed as mean ± SEM. * indicates statistical significance vs. 12 wk time point.

Table 2. Cardiac function parameters from baseline and 12 wk postembolization

Cardiac function parameters	Baseline	12 wk postembolization		*P* value
		Placebo	GHRH-A	
Integrated cardiac function				
EF, %	41.1 ± 1.5	50.6 ± 3.0*	51.6 ± 3.4*	0.0001
Ea/Ees ratio	3.05 ± 0.31	3.17 ± 2.40	2.40 ± 0.37	0.47
SV/BSA, mL/m^2	43.7 ± 0.5	55.1 ± 6.1*	51.1 ± 2.6*	0.002
Preload				
EDP, mmHg	13.7 ± 1.0	21.2 ± 2.9*	23.0 ± 3.5*	0.002
EDV/BSA, mL/m^2	106.4 ± 0.6	110.1 ± 5.3	101.7 ± 4.1	0.67
Afterload				
Ea, mmHg/mL	2.5 ± 0.5	1.8 ± 0.2*	1.9 ± 0.2*	0.02
SBP, mmHg	85.2 ± 3.3	89.4 ± 5.1	92.2 ± 8.2	0.95
DBP, mmHg	56.0 ± 2.5	61.3 ± 5.0	65.9 ± 8.5	0.82
Contractility				
dP/dt max, mmHg/s	803.9 ± 43.7	840.0 ± 54.2	983.3 ± 103.2	0.19
ESV/BSA, mL/m^2	62.8 ± 0.6	54.7 ± 5.7*	49.3 ± 4.7*	0.0002
PRSW, mmHg	32.9 ± 4.3	37.3 ± 4.9	39.0 ± 2.9	0.25
ESPVR, mmHg/mL	0.9 ± 0.1	0.6 ± 0.1	0.5 ± 0.1	0.16
Lusitropy				
EDP/EDV ratio/BSA, mmHg/mL/m^2	0.12 ± 0.01	0.20 ± 0.03*	0.22 ± 0.03*	0.002
Tau, ms	45.8 ± 1.9	71.6 ± 6.3*	67 ± 9.2	0.001
Ventricular morphology				
Relative wall thickness	0.3 ± 0.01	0.5 ± 0.05*	0.5 ± 0.04*	0.003
LVED mass/BSA, g/m^2	84.4 ± 0.6	116.8 ± 5.9*	121.7 ± 3.2*	0.002

This table shows the establishment of the CKD-induced model prior to treatment. The values at 12 wk postembolization are divided according to the subsequent treatment. DBP, diastolic blood pressure; dP/dt max, maximal value of the first temporal derivative of the ventricular pressure; Ea, arterial elastance; EDP/EDV ratio/BSA, end-diastolic pressure–volume ratio, index for body surface area; EDPVR, end-diastolic pressure–volume relationship; EF, ejection fraction; ESPVR, end-systolic pressure–volume relationship; ESV/BSA, end-systolic volume, index for body surface area; LVED mass/BSA, left ventricular end-diastolic mass, index for body surface; PRSW, preload recruitable stroke work relation; SBP, systolic blood pressure; SV/BSA, stroke volume, index for body surface area; tau, left ventricular diastolic time constant. *P* values refer to analysis within groups throughout the model establishment, paired *t* test. No statistical differences between groups at 12-wk postembolization time point. All data are expressed as mean ± SEM. * indicates statistical significance compared to Baseline. Two-way ANOVA; *P* values are shown in the last column.

assessed the expression of *CCL2* in the myocardium of control swine, and swine with CKD-induced HFpEF that were treated with placebo or GHRH-A. Placebo-treated swine had significantly elevated levels of *CCL2* compared to control and GHRH-A–treated animals. GHRH-A treatment returned *CCL2* expression to control levels (*SI Appendix*, Fig. S5).

Discussion

This randomized, blinded, placebo-controlled, preclinical study tested the effectiveness of a synthetic, potent GHRH-A to improve the HFpEF phenotype compared to placebo, in a large-animal model of CKD-induced HFpEF. These encouraging results demonstrate that GHRH-A produced a substantial improvement in cardiac diastolic function in animals with established CKD-induced HFpEF. In humans, HFpEF is a common, but particularly challenging disorder, lacking effective treatments. Accordingly, this study has important translational and clinical implications for the important unmet clinical need of HFpEF.

To accomplish this study, we developed a large-animal model of HFpEF. To create this model, we performed renal artery embolization in swine (19) leading to the development of acute kidney injury. The animals also had accompanying hyperkalemia and volume overload that was managed with daily diuretic (furosemide) treatment lasting ∼2 wk, and subsequent administration as needed, while their renal function improved (via hyperfiltration of the remnant kidney) and stabilized.

In our large-animal model, hypertrophy of the LV and SW elevation were evident, similar to that described in the CKD-HFpEF phenotype (11). Ventricular tachycardia was stimulated in two animals, one prior to treatment and one following randomization to the placebo treatment, corroborating potential structural (proarrhythmic) changes in the myocardium. Together, these preclinical findings support ongoing translational development of this class of agents for human HFpEF.

GHRH-A reparative effects on the myocardium in the setting of HFpEF likely occur through multiple mechanisms (28), including antiapoptotic effects via inhibition of ERK1/2 and PI3K/Akt signaling associated with elevated Bcl-2 and reduced Bax:Bcl-2 ratio (14, 17), stimulation of cardiac progenitor proliferation (14, 29), inhibition of hypertrophy, including Gq signaling and downstream pathways (30), and reduced inflammation, specifically plasma levels of IL-2, IL-6, and TNF-α, reduced expression of profibrotic pathway genes (14), and better organized collagen deposition (14). In a mouse model of angiotensin II-induced HFpEF, GHRH-A inhibited cardiomyocyte sarcomere and contractile dysfunction, preventing Ca^{2+} leak from the SR and improving sarcomere relaxation and calcium handling (18). A substantial benefit of GHRH-A on the restoration of the diastolic cardiac function was demonstrated in the treated animals of this study, including EDP (ventricular preload) and end-diastolic/pressure–volume ratio (EDP/EDV, a measure of passive chamber stiffness). There was a trend toward reduced hypertrophy following a 4- to 6-wk treatment with GHRH-A. The ability of GHRH-A to further improve or offset deterioration in LV hypertrophy will be tested in future experiments using longer durations or increased doses of GHRH-A. The potential anti-arrhythmogenic effect, independent of the scar

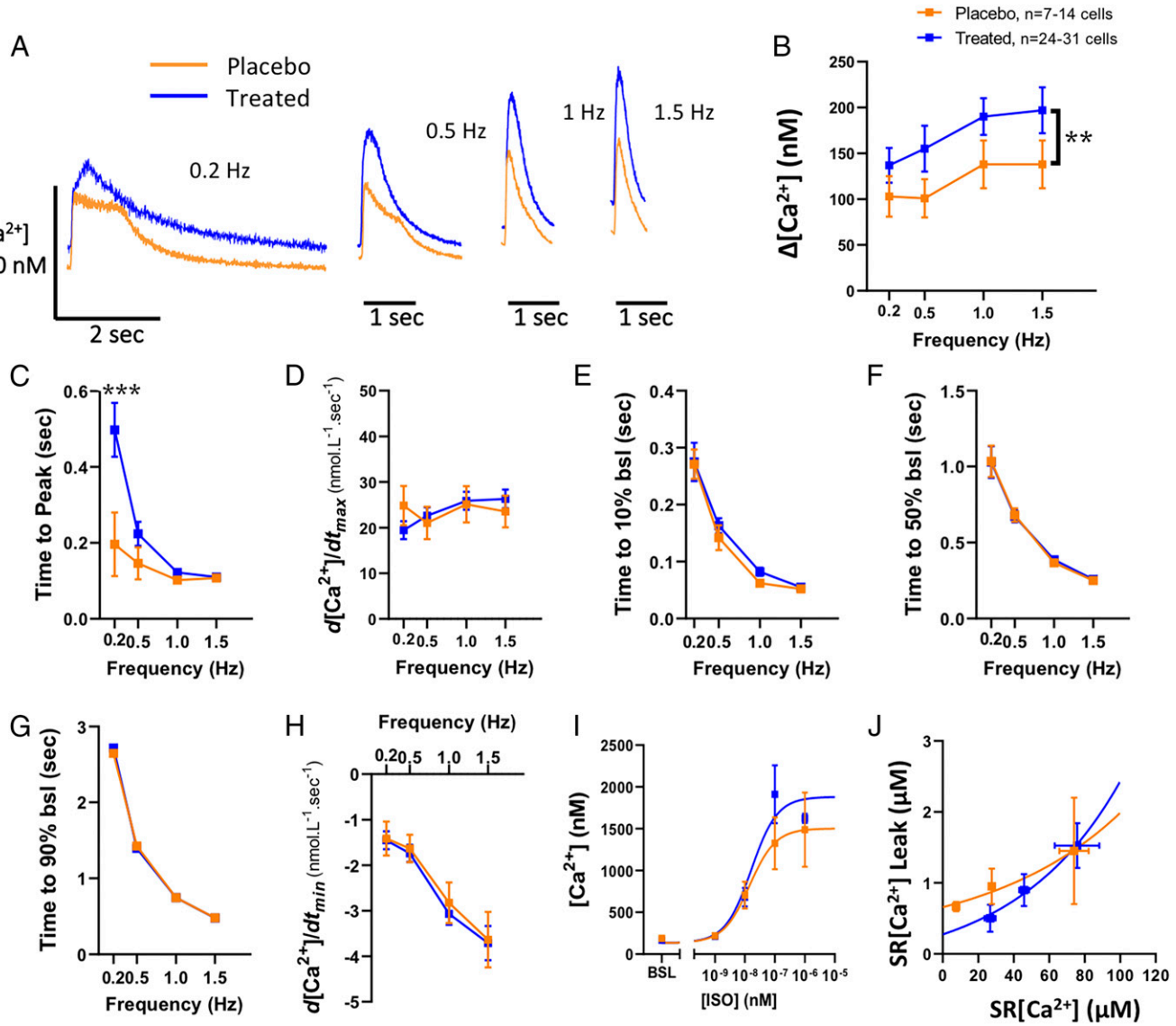

Fig. 3. Calcium handling in cardiomyocytes. (*A*) Representative individual traces of intracellular [Ca^{2+}] comparing placebo- vs. GHRH-A–treated cardiomyocytes electric field-stimulated at 0.2, 0.5, 1, and 1.5 Hz. (*B*) Average [Ca^{2+}] transient amplitude in placebo and GHRH-A groups. (*C*) Average of the time elapsed from the electric stimulus to the peak of the [Ca^{2+}] transient. $^{**}P = 0.009$. (*D*) Maximum [Ca^{2+}] rise velocity. (*E*) Decay rate from the [Ca^{2+}] transient peak to 10% of the way to baseline (time to 10% bsl). (*F*) [Ca^{2+}] decay rate assessed as time to 50% bsl. (*G*) [Ca^{2+}] decay as time to 90% bsl. (*H*) Maximum [Ca^{2+}] decay velocity. (*I*) Response of cardiomyocyte intracellular [Ca^{2+}] transient amplitude to increasing dose of isoproterenol. (*J*) Sarcoplasmic reticulum (SR) Ca^{2+} leak–SR Ca^{2+} load relationship. $^{***}P < 0.001$, two-way ANOVA. All data are expressed as mean ± SEM.

reduction seen with GH therapy (31), was also seen with this GHRH analog; this is at present a poorly understood effect, and further studies will be conducted to elucidate underlying mechanisms.

We explored the relative contribution of myocardial fibrosis vs. cardiomyocyte stiffness in the reduced myocardial compliance seen in this swine model of CKD-induced HFpEF. The type and prevalence of interstitial fibrosis is an important parameter for myocardial recovery in ischemic and dilated cardiomyopathy (32). However, the absence of increased fibrosis in these hearts suggest that GHRH-A can improve compliance of stiff myocardium at the level of the cardiomyocyte even in settings where reduction of fibrosis is not evident. GHRH-A administration could have further benefits if myocardial fibrosis played a role as has been shown in rat (13–15, 33) and swine (12) models of ICM.

Further evidence of a direct effect of GHRH-A on cardiomyocytes is the increased titin phosphorylation seen in GHRH-A–treated animals. A molecular hallmark of HFpEF, recapitulated in our model, is hypophosphorylation of titin (22) in the myocardium, which may result from reduced myocardial protein kinase G activity induced by nitroso-redox imbalance (34–37). Reducing titin phosphorylation/stiffness has shown beneficial effects in animal models of HFpEF (38–40) and is a target in human clinical trials testing sodium-glucose-cotransporter (SGLT)-2 inhibitors (41, 42). The GHRH-A–mediated reduction in myocardial pro-BNP and inflammatory markers (14), including CCL2 (*SI Appendix*, Fig. S5), suggest that GHRH-A functions to decrease myocardial stress and inflammation. Together, these effects could reduce cardiomyocyte apoptosis as seen following GHRH-A treatment in rat models of ICM (15), potentially restoring the balance between cardiomyocyte loss and replacement

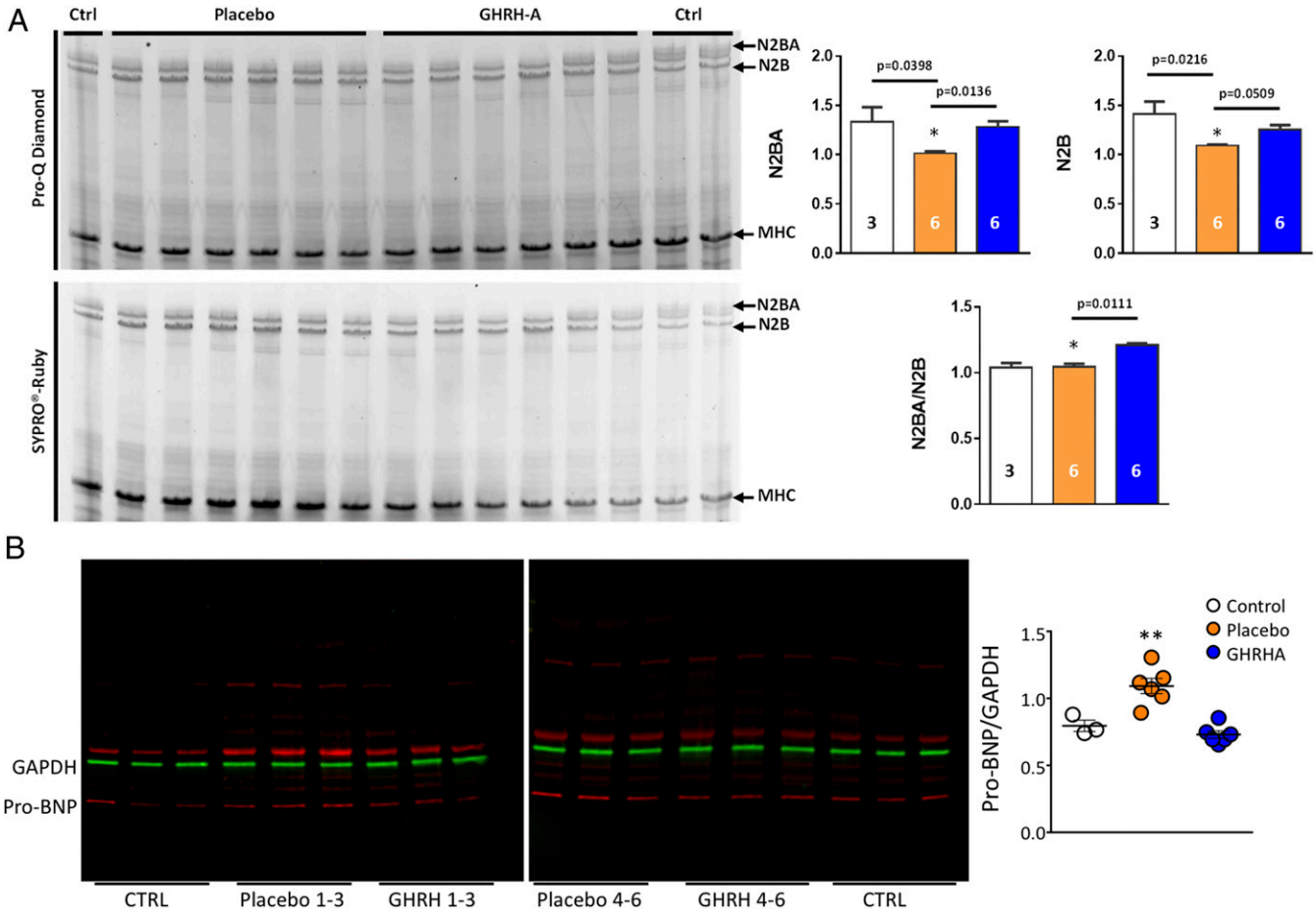

Fig. 4. Titin and pro-BNP expression in myocardium. (*A*) Expression and phosphorylation of titin isoforms. Representative image of 1% agarose gel electrophoresis with SYPRO Ruby and ProQ Diamond phosphoprotein stain for titin analysis of LV. Bar graphs show relative hypophosphorylation of both N2BA and N2B isoforms, as well as the N2BA/N2B ratio in the control (white; $n = 3$), placebo (orange; $n = 6$), and GHRH- A (blue; $n = 6$) groups. The relative phosphorylated titin expression is the average of triplicate values. All data are expressed as mean ± SEM. $^*P < 0.05$ by Kruskal–Wallis test. (*B*) Expression of pro-BNP in the myocardium. Representative Western blot for pro-BNP expression from swine myocardial biopsies from control (lanes 1 to 3 and 16 to 18), placebo-treated (lanes 4 to 6 and 10 to 12), and GHRH-A–treated (lanes 7 to 9 and 13 to 15). Quantification of Western blots for all samples; control ($n = 3$), placebo treated ($n = 6$), and GHRH-A treated ($n = 6$). $^{**}P = 0.003$ placebo vs. GHRH-A by Dunn's multiple-comparisons test.

(17). These important molecular changes further support the investigation of GHRH-As as a therapeutic for HFpEF.

In summary, together our findings reveal that GHRH-A administration in a large-animal model of HFpEF has a constellation of salutary physiologic and molecular effects. GHRH-A was well tolerated in the animals and improved diastolic dysfunction. In addition, activating myocardial GHRH receptors reduced myocardial pro-BNP, improved titin stiffness, and reduced myocardial CCL2 independently of reducing fibrosis. Accordingly, these findings reveal a potential therapeutic approach for HFpEF and cardiorenal syndromes and provide rationale for further clinical translational studies.

Materials and Methods

The study was conducted in a blinded fashion. All animal protocols were approved by the University of Miami Institutional Animal Care and Use Committee. Female Yorkshire swine (30 to 35 kg) underwent catheter-induced embolization with polyvinyl alcohol particles (19, 43) (150 to 250 μm; Boston Scientific) and 100% ethanol infusion to produce the 5/6 nephrectomy CKD model. Postembolization arteriograms were performed to assess the residual renal flow to the embolized and remnant kidney. Twelve weeks postembolization, animals were randomized to receive daily subcutaneous injections of GHRH-A ($n = 8$, MR-409; 30 μg/kg dissolved in DMSO/propylene glycol/PBS) or placebo ($n = 8$, GHRH-A diluent) for 4 to 6 wk.

The GHRH-A MR-409 [N-Me-Tyr1, D-Ala2, Orn12, 21, Abu15, Nle27, Asp28-GHRH (1–29) $NHCH_3$] was synthetized by solid-phase methods and purified by HPLC, as described previously (13).

Renal anatomical structure and perfusion was evaluated by renal MRI (20) (3.0T clinical scanner; Magnetom; Siemens AG). Follow-up evaluations were done weekly in the initial month and monthly throughout the GHRH-A treatment or placebo. Animals were studied for a total of 16 to 18 wk in a blinded manner.

Cardiac MRI was conducted at the Interdisciplinary Stem Cell Institute to evaluate cardiac function Siemens Trio 3T Tim with Syngo MR Software using a 16-channel body surface coil with electrocardiography (ECG) gating and short breath-hold acquisitions. Cardiac evaluation included ECG-gated cine, first-pass gadolinium delayed hyper enhancement images and tagging (44).

Kidney functional laboratory measurements, including serum creatinine and BUN, protein and creatinine in urine, hematology, and chemistry were performed for validation of the CKD model at baseline, 12-, and 16- to 18-wk postembolization time points.

Animal Model. The renal embolization-induced 5/6 nephrectomy was performed in 36 Yorkshire swine. This procedure to create a remnant kidney model of chronic kidney disease carries a high mortality rate, as previously described (19). Sixteen animals successfully completed the study and were included in this analysis. Twenty animals died before initiation of the

treatment, the majority in the first 2 initial weeks, as expected. Three had complications during the embolization procedure because of arteriovenous malformation, myocardial infarction, and anaphylaxis, respectively. After the procedure, 1 animal died as a complication of a central line placement, and 12 died secondary to acute kidney injury. One animal died at 12 wk during the electrical stimulation procedure, which reproduced a ventricular tachycardia that converted to ventricular fibrillation that did not respond to treatment.

Hemodynamic Assessment. Pressure–volume (PV) loops were performed at baseline, 12 wk postembolization, and at the end of the study at 16 to 18 weeks, using a micromanometer-conductance catheter (VENTRI CATH 507 for Large Animals; AD Instruments) (45). Following Seldinger technique, the catheter was placed within the LV and steady-state PV loops were performed. Subsequently, the inferior vena cava was occluded with a balloon to determine end-diastolic pressure–volume relationship (EDPVR) and end-systolic pressure–volume relationship (ESPVR). Data were acquired after the animals were given time to stabilize.

The peripheral mean arterial blood pressure was obtained by an indirect and noninvasive methodology. With the pig in a lateral recumbent position, the arterial pulse was located in the medial aspect of the foreleg between the elbow and the carpal joint. A pediatric blood pressure cuff (Hewlett Packard) was placed around the leg distal to the elbow. Data were collected at baseline and at different timepoints postembolization: 30 min, 24 and 72 h, and 1, 2, 4, 6, 8, 11, and 12 wk.

Electrophysiologic Assessment. Programmed electrical stimulation pacing was performed at twice diastolic threshold using an electro stimulator triggered by a personal computer, via a bipolar catheter placed intravenously in the right ventricular apex and left ventricular apex. For a refractory assessment period, a drive train sequence of 8 to 10 pulses (S1) is delivered at S1S1 cycle length 400 ms, followed by the delivery of premature extra stimuli (S2) at 340 ms, 320 ms, and reduced in 20-ms decrements to the point where the S2 impulse does not capture, i.e., at the ventricular effective refractory period. The induction of sustained ventricular arrhythmias was performed in each animal at 12 wk and 16 to 18 wk (end of study) time points after embolization. This stimulation was performed in the right and left ventricles.

Calcium Measurements. Cardiomyocytes were isolated and prepared from swine heart biopsies by adapting a previously described protocol (46). Briefly, left ventricular biopsies were collected from the swine in the operating room at the 16 to 18 wk time point. Specimens were kept in an ice-cold cardioplegic buffer (in mmol/L: 50 KH_2PO_4, 8 $MgSO_4$, 10 Hepes, 5 adenosine, 140 glucose, 100 mannitol, 10 taurine) and processed within 10 min. Myocardial tissues were washed twice and then minced into small pieces (~3 mm). Tissue chunks were transferred into a digestion device and then subjected to sequential (six steps) enzymatic digestion (at 37 °C) using collagenase type V (Worthington Biochemical Corporation) at 250 U/mL and protease type XXIV (Sigma-Aldrich) at 4 U/mL, in a digestion buffer containing the following (in mmol/L): 1.2 $MgSO_4$, 10 glucose, 20 taurine, 113 NaCl, 4.7 KCl, 0.6 KH_2PO_4, 0.6 NaH_2PO_4, 12 $NaHCO_3$, 12 $KHCO_3$, 4 Na-pyruvate, and 10 butadiene monoxime. Supernatants containing the cardiomyocytes were collected in digestion buffer with 0.5% bovine serum albumin (Sigma-Aldrich). The cells were subjected to a sequential extracellular Ca^{2+} restoration in Tyrode's buffer containing the following (in mmol/L): 144 NaCl, 1 $MgCl_2$, 10 Hepes, 5.6 glucose, 5 KCl, and 1.2 NaH_2PO_4 (adjusted to a pH 7.4 with NaOH). Finally, cardiomyocytes were resuspended in Tyrode's buffer containing 1.8 mmol/L $CaCl_2$ at room temperature until being used.

Intracellular Ca^{2+} was measured using the Ca^{2+}-sensitive dye Fura-2 and a dual-excitation (340/380 nm) spectrofluorometer (IonOptix). Cardiomyocytes were incubated with 2.5 μmol/L Fura-2 for 15 min at room temperature and then washed with fresh regular Tyrode's solution for at least 10 min. Next, cardiomyocytes were placed in a perfusion chamber adapted to the stage of an inverted Nikon eclipse TE2000-U fluorescence microscope. Cells were superfused with a Tyrode's buffer at 37 °C and Fura-2 fluorescence was acquired at an emission wavelength of 515 ± 10 nm. The cardiomyocytes were electric field-paced (20 V) at different frequencies from 0.2 to 1.5 Hz. The calibration was performed in cardiomyocytes "ex vivo," superfusing a free Ca^{2+} and then a Ca^{2+} saturating (5 mmol/L) solution, both containing 10 μmol/L ionomycin (Sigma) until reaching a minimal (R_{min}) or a maximal (R_{max}) ratio value, respectively. $[Ca^{2+}]_i$ was calculated as described previously using the following equation:

$$[Ca^{2+}]_i = K_d \times \frac{S_{f2}}{S_{b2}} \times \frac{(R - R_{min})}{(R_{max} - R)}.$$

K_d (dissociation constant) in adult myocytes was taken as 224 nmol/L. The scaling factors S_{f2} and S_{b2} were extracted from calibration as previously described (47). $\Delta[Ca^{+2}]_i$ amplitude was considered as follows: peak $[Ca^{+2}]_i$ – resting $[Ca^{+2}]_i$.

SR Ca^{2+} Leak Assessment. SR Ca^{2+} leak was assessed using tetracaine as previously described (47). Briefly, after stopping cardiomyocyte pacing, the superfusing buffer was immediately switched to a $0Na^+/0Ca^{2+}$ Tyrode's buffer containing the following (in mmol/L): 144 LiCl, 1 $MgCl_2$, 10 Hepes, 5.6 glucose, 5 KCl, 10 EGTA (pH adjusted up to 7.4 with LiOH) during ~30 s to prevent Ca^{2+} fluxes through the sarcolemma. Thus, the intracellular Ca^{2+} was maintained approximately unaltered and the cytosolic $[Ca^{2+}]$ reached a steady state due to a balance between the SR Ca^{2+} fluxes (Ca^{2+} uptake and Ca^{2+} leak). Then a $0Na^+/0Ca^{2+}$ Tyrode's solution with 1 mM tetracaine (Sigma-Aldrich) was applied for at least 60 s. Under this condition, the SR Ca^{2+} leak is blocked and then allowing the Ca^{2+} uptake to reduce cytosolic $[Ca^{2+}]$ until reaching a minimum in the Fura-2 ratio. Following, the superfusing solution was switched back to tetracaine-free $0Na^+/0Ca^{2+}$ Tyrode's buffer and SR Ca^{2+} content was assessed as described previously (47) by a 20 mmol/L caffeine challenge. SR Ca^{2+} contents were calculated considering that SR represents 3.5% and cytosol 65% of the myocyte volume as previously described (48). The following equation from Shannon et al. (48) was used:

$$SR[Ca^{2+}] = [Ca^{2+}]_{caff} + \frac{\beta_{max-SR} \times [Ca^{2+}]_{caff}}{[Ca^{2+}]_{caff} + K_{d-SR}}.$$

$SR[Ca^{2+}]$ is the SR Ca^{2+} content, $[Ca^{2+}]_{caff}$ is the SR Ca^{2+} released by caffeine, $\beta_{max\text{-}SR}$ and $K_{d\text{-}SR}$ are the usual Michaelis parameters for SR Ca^{2+} binding.

The observed decrease in the Fura-2 ratio in the presence of tetracaine compared to the ratio prior to applying tetracaine was considered the Ca^{2+} leak for a particular myocyte (expressed in micromoles per liter). SR Ca^{2+} leak-SR $[Ca^{2+}]$ pairs were grouped by similar SR Ca^{2+} load ($SR[Ca^{2+}]$), plotted, and fitted by an exponential growth function using GraphPad Prism software (version 8.4.3; GraphPad Software). Measurements were carried out at 37 °C.

Western Blotting.

Titin assessment. For detection of titin, LV samples were solubilized and electrophoresed using 1% agarose gels as described with minor modifications (49). Briefly, LV samples were flash frozen in liquid nitrogen and solubilized between glasses pestles cooled in liquid nitrogen. Samples were primed at −20 °C for a minimum of 20 min, then suspended in 50% urea buffer (in mol/L: 8 urea, 2 thiourea, 0.05 Tris·HCl, 0.075 dithiothreitol with 3% SDS, and 0.03% bromophenol blue, pH 6.8) and 50% glycerol with protease inhibitors (in mmol/L: 0.04 E64, 0.16 leupeptin, and 0.2 PMSF) at 60 °C for 10 min. Then the samples were centrifuged at 12,500 rpm for 5 min, aliquoted, flash frozen in liquid nitrogen, and stored at −80 °C (50).

Total titin phosphorylation was analyzed using the fluorescence-based phosphoprotein stain ProQ diamond (Invitrogen) in comparison to the total protein stain Sypro Ruby (Invitrogen). The gels were stained for 60 min with ProQ Diamond (Molecular Probes). Thereafter, the gels were washed and subsequently stained with SYPRO Ruby (Molecular Probes). Staining and imaging procedure were performed according to the manufacturer's instructions, scanned using a commercial scanner (GE Corporation), and analyzed with ImageJ software.

Titin isoform expression was determined in LV samples from control group (n = 3), placebo group (n = 6), and GHRH-A–treated group (n = 6) in triplicate gels.

Pro-BNP assessment. Flash-frozen LV samples were homogenized using a Pyrex glass-glass homogenizer in liquid nitrogen and urea buffer containing: 8 M urea, 2 M thiourea, 3% SDS, 0.03% bromophenol blue, and 0.05 M Tris, pH 6.8. Glycerol (50%) was added. Samples were centrifuged at 12,500 rpm for 5 min. Supernatants were collected and sampled for protein concentration by Bradford assay (Thermo Scientific). Samples (15 μg protein/well) and dual molecular weight ladders (Precision Plus Protein Dual Color Standards; Bio-Rad) were loaded on a 4 to 20% gradient agarose gel, electrophoresed, and transferred to nitrocellulose membranes (Bio-Rad Laboratories). Membranes were blocked with TBS + Rockland blocking buffer MB-070 (1:1) for 1 h at room temperature. Immunoblot analysis was performed using rabbit polyclonal antibodies against collagen I and collagen III (Abcam: ab34710 and ab7778, respectively), mouse monoclonal antibody

for pro-BNP (Abcam: ab239514), and mouse monoclonal antibody for GAPDH (Cell Signaling; #97166S) as internal loading control (overnight incubation at 4 °C). Detection was carried out by incubating with the fluorescent dye-conjugated antibodies anti-rabbit IRDye 680RD and 800CW; LI-COR; 925-68071 and 925-32211) and anti-mouse IgG (IRDye 680RD and 800CW; LI-COR; 925-68070 and 925-32210) for 1 h at room temperature. Images were acquired by an Odyssey infrared imaging system (LI-COR Biosciences). Detection and quantification of band intensities were analyzed using the Image Studio Litesoftware (LI-COR) and ImageJ.

Picro-Sirius Red Staining. Total collagen content was assessed using Picro-Sirius Red stain kit (Abcam; ab245887) according to the manufacturer's instructions. The collagen content was measured as the Sirius Red intensity normalized to the total myocardial area using light microscopy images. For quantification purposes, the heart sections were digitally scanned at 10× magnification (Olympus scanner VS120), and Adobe Photoshop CS3 was used to measure collagen content area across the entire digital slide following ImageJ protocol.

Quantitative RT-PCR. Samples from LVs were homogenized and isolated using the RNAEasy kit (Qiagen) and transcribed into complementary DNA with the use of the synthesis kit (Applied Biosystems). Quantitative PCRs were carried out on a Bio-Rad CFX96 Real-Time PCR system (Bio-Rad). All samples were run in duplicate and normalized to HPRT1: Ss03388273_m1 TaqMan gene expression with specific probe against CCL2: Ss03394377_m1.

Statistical Analysis. All data are expressed as mean ± SEM. Data distribution was assessed with Pearson normality test. Paired *t* test was performed to compare two groups at distinct time points. Kruskal–Wallis tests were used for analysis of Western blots. Two-way ANOVA was used for multiple time points or groups and multiple comparisons were estimated using the Bonferroni and Tukey corrections and expressed as mean ± SEM for normally distributed data. Mann–Whitney test was used to evaluate continuous variables nonnormally distributed and described by median and interquartile range. All statistics used two-sided tests with $\alpha = 0.05$. Values were considered significant when $P < 0.05$.

Data Availability. All study data are included in the article and *SI Appendix*.

ACKNOWLEDGMENTS. This study was funded by NIH Grants 1R01 HL107110, 1R01 HL13735 and by The Lipson Family (to J.M.H.). J.M.H. is also supported by NIH Grants 5UM1 HL113460, 1R01 HL134558, 5R01429 CA136387, and HHSN268201600012I; Department of Defense Grant W81XWH-19-PRMRP-CTA; and The Soffer Family and Starr Foundations.

1. M. A. Pfeffer, A. M. Shah, B. A. Borlaug, Heart failure with preserved ejection fraction in perspective. *Circ. Res.* **124**, 1598–1617 (2019).
2. B. Pieske *et al*., How to diagnose heart failure with preserved ejection fraction: The HFA-PEFF diagnostic algorithm: A consensus recommendation from the Heart Failure Association (HFA) of the European Society of Cardiology (ESC). *Eur. Heart J.* **40**, 3297–3317 (2019).
3. C. S. P. Lam, A. A. Voors, R. A. de Boer, S. D. Solomon, D. J. van Veldhuisen, Heart failure with preserved ejection fraction: From mechanisms to therapies. *Eur. Heart J.* **39**, 2780–2792 (2018).
4. B. Pitt *et al*.; TOPCAT Investigators, Spironolactone for heart failure with preserved ejection fraction. *N. Engl. J. Med.* **370**, 1383–1392 (2014).
5. S. Yusuf *et al*.; CHARM Investigators and Committees, Effects of candesartan in patients with chronic heart failure and preserved left-ventricular ejection fraction: The CHARM-preserved trial. *Lancet* **362**, 777–781 (2003).
6. J. G. Cleland *et al*.; PEP-CHF Investigators, The perindopril in elderly people with chronic heart failure (PEP-CHF) study. *Eur. Heart J.* **27**, 2338–2345 (2006).
7. B. M. Massie *et al*.; I-PRESERVE Investigators, Irbesartan in patients with heart failure and preserved ejection fraction. *N. Engl. J. Med.* **359**, 2456–2467 (2008).
8. J. A. Regan *et al*., A mouse model of heart failure with preserved ejection fraction due to chronic infusion of a low subpressor dose of angiotensin II. *Am. J. Physiol. Heart Circ. Physiol.* **309**, H771–H778 (2015).
9. G. G. Schiattarella *et al*., Nitrosative stress drives heart failure with preserved ejection fraction. *Nature* **568**, 351–356 (2019).
10. S. J. Shah *et al*., Research priorities for heart failure with preserved ejection fraction: National Heart, Lung, and Blood Institute Working Group summary. *Circulation* **141**, 1001–1026 (2020).
11. S. J. Shah *et al*., Phenomapping for novel classification of heart failure with preserved ejection fraction. *Circulation* **131**, 269–279 (2015).
12. L. L. Bagno *et al*., Growth hormone-releasing hormone agonists reduce myocardial infarct scar in swine with subacute ischemic cardiomyopathy. *J. Am. Heart Assoc.* **4**, e001464 (2015).
13. R. Cai *et al*., Synthesis of new potent agonistic analogs of growth hormone-releasing hormone (GHRH) and evaluation of their endocrine and cardiac activities. *Peptides* **52**, 104–112 (2014).
14. R. M. Kanashiro-Takeuchi *et al*., New therapeutic approach to heart failure due to myocardial infarction based on targeting growth hormone-releasing hormone receptor. *Oncotarget* **6**, 9728–9739 (2015).
15. R. M. Kanashiro-Takeuchi *et al*., Activation of growth hormone releasing hormone (GHRH) receptor stimulates cardiac reverse remodeling after myocardial infarction (MI). *Proc. Natl. Acad. Sci. U.S.A.* **109**, 559–563 (2012).
16. D. Caicedo, O. Díaz, P. Devesa, J. Devesa, Growth hormone (GH) and cardiovascular system. *Int. J. Mol. Sci.* **19**, 290 (2018).
17. J. M. Hare, Oxidative stress and apoptosis in heart failure progression. *Circ. Res.* **89**, 198–200 (2001).
18. R. A. Dulce *et al*, Synthetic agonist of growth hormone-releasing hormone as novel treatment for heart failure with preserved ejection fraction. https://doi.org/10.1101/2020.02.28.967000 (28 February 2020).
19. S. Misra *et al*., The porcine remnant kidney model of chronic renal insufficiency. *J. Surg. Res.* **135**, 370–379 (2006).
20. F. C. McCall *et al*., Myocardial infarction and intramyocardial injection models in swine. *Nat. Protoc.* **7**, 1479–1496 (2012).
21. D. R. Gonzalez, A. V. Treuer, J. Castellanos, R. A. Dulce, J. M. Hare, Impaired S-nitrosylation of the ryanodine receptor caused by xanthine oxidase activity contributes to calcium leak in heart failure. *J. Biol. Chem.* **285**, 28938–28945 (2010).
22. A. Borbély *et al*., Hypophosphorylation of the Stiff N2B titin isoform raises cardiomyocyte resting tension in failing human myocardium. *Circ. Res.* **104**, 780–786 (2009).
23. S. Wiese *et al*., Gene expression of brain natriuretic peptide in isolated atrial and ventricular human myocardium: Influence of angiotensin II and diastolic fiber length. *Circulation* **102**, 3074–3079 (2000).
24. S. Epelman, P. P. Liu, D. L. Mann, Role of innate and adaptive immune mechanisms in cardiac injury and repair. *Nat. Rev. Immunol.* **15**, 117–129 (2015).
25. P. E. Kolattukudy, J. Niu, Inflammation, endoplasmic reticulum stress, autophagy, and the monocyte chemoattractant protein-1/CCR2 pathway. *Circ. Res.* **110**, 174–189 (2012).
26. D. L. Mann, Innate immunity and the failing heart: The cytokine hypothesis revisited. *Circ. Res.* **116**, 1254–1268 (2015).
27. L. Zhou *et al*., Monocyte chemoattractant protein-1 induces a novel transcription factor that causes cardiac myocyte apoptosis and ventricular dysfunction. *Circ. Res.* **98**, 1177–1185 (2006).
28. A. V. Schally *et al*., Actions and potential therapeutic applications of growth hormone-releasing hormone agonists. *Endocrinology* **160**, 1600–1612 (2019).
29. V. Florea *et al*., Agonists of growth hormone-releasing hormone stimulate self-renewal of cardiac stem cells and promote their survival. *Proc. Natl. Acad. Sci. U.S.A.* **111**, 17260–17265 (2014).
30. I. Gesmundo *et al*., Growth hormone-releasing hormone attenuates cardiac hypertrophy and improves heart function in pressure overload-induced heart failure. *Proc. Natl. Acad. Sci. U.S.A.* **114**, 12033–12038 (2017).
31. K. V. Stamatis, M. Kontonika, E. P. Daskalopoulos, T. M. Kolettis, Electrophysiologic effects of growth hormone post-myocardial infarction. *Int. J. Mol. Sci.* **21**, 918 (2020).
32. J. M. Hare *et al*., Ischemic cardiomyopathy: Endomyocardial biopsy and ventriculographic evaluation of patients with congestive heart failure, dilated cardiomyopathy and coronary artery disease. *J. Am. Coll. Cardiol.* **20**, 1318–1325 (1992).
33. R. M. Kanashiro-Takeuchi *et al*., Cardioprotective effects of growth hormone-releasing hormone agonist after myocardial infarction. *Proc. Natl. Acad. Sci. U.S.A.* **107**, 2604–2609 (2010).
34. L. van Heerebeek *et al*., Low myocardial protein kinase G activity in heart failure with preserved ejection fraction. *Circulation* **126**, 830–839 (2012).
35. J. M. Hare, Nitroso-redox balance in the cardiovascular system. *N. Engl. J. Med.* **351**, 2112–2114 (2004).
36. J. M. Hare, J. S. Stamler, NO/redox disequilibrium in the failing heart and cardiovascular system. *J. Clin. Invest.* **115**, 509–517 (2005).
37. P. Varghese *et al*., beta(3)-adrenoceptor deficiency blocks nitric oxide-dependent inhibition of myocardial contractility. *J. Clin. Invest.* **106**, 697–703 (2000).
38. M. Schwarzl *et al*., A porcine model of hypertensive cardiomyopathy: Implications for heart failure with preserved ejection fraction. *Am. J. Physiol. Heart Circ. Physiol.* **309**, H1407–H1418 (2015).
39. R. E. Slater *et al*., Metformin improves diastolic function in an HFpEF-like mouse model by increasing titin compliance. *J. Gen. Physiol.* **151**, 42–52 (2019).
40. S. F. Nagueh, Heart failure with preserved ejection fraction: Insights into diagnosis and pathophysiology. *Cardiovasc. Res.*, 10.1093/cvr/cvaa228. (2020).

41. D. Kolijn *et al*., Empagliflozin improves endothelial and cardiomyocyte function in human heart failure with preserved ejection fraction via reduced pro-inflammatory-oxidative pathways and protein kinase Gα oxidation. *Cardiovasc. Res.*, 10.1093/cvr/cvaa123 (2020).
42. M. Scheffer *et al*., Stratified treatment of heart failure with preserved ejection fraction: Rationale and design of the STADIA-HFpEF trial. *ESC Heart Fail.*, 10.1002/ehf2.13055 (2020).
43. G. P. Siskin, K. Dowling, R. Virmani, R. Jones, D. Todd, Pathologic evaluation of a spherical polyvinyl alcohol embolic agent in a porcine renal model. *J. Vasc. Interv. Radiol.* **14**, 89–98 (2003).
44. A. R. Williams *et al*., Enhanced effect of combining human cardiac stem cells and bone marrow mesenchymal stem cells to reduce infarct size and to restore cardiac function after myocardial infarction. *Circulation* **127**, 213–223 (2013).
45. M. Natsumeda *et al*., A combination of allogeneic stem cells promotes cardiac regeneration. *J. Am. Coll. Cardiol.* **70**, 2504–2515 (2017).
46. R. Coppini *et al*., Isolation and functional characterization of human ventricular cardiomyocytes from fresh surgical samples. *J. Vis. Exp.* **2014**, 51116 (2014).
47. R. A. Dulce *et al*., Hydralazine and organic nitrates restore impaired excitation-contraction coupling by reducing calcium leak associated with nitroso-redox imbalance. *J. Biol. Chem.* **288**, 6522–6533 (2013).
48. T. R. Shannon, K. S. Ginsburg, D. M. Bers, Quantitative assessment of the SR Ca^{2+} leak-load relationship. *Circ. Res.* **91**, 594–600 (2002).
49. H. L. Granzier *et al*., Deleting titin's I-band/A-band junction reveals critical roles for titin in biomechanical sensing and cardiac function. *Proc. Natl. Acad. Sci. U.S.A.* **111**, 14589–14594 (2014).
50. S. Lahmers, Y. Wu, D. R. Call, S. Labeit, H. Granzier, Developmental control of titin isoform expression and passive stiffness in fetal and neonatal myocardium. *Circ. Res.* **94**, 505–513 (2004).